

## Deep Learning-Enabled Prediction of Geoeffective CMEs Using SOHO and SDO Observations

Zhaoxin Yan<sup>1,2</sup> · Jason T. L. Wang<sup>1,2</sup> ·  
Haimin Wang<sup>1,3,4</sup> · Harim Lee<sup>1,3</sup> ·  
Ju Jing<sup>1,3,4</sup> · Yan Xu<sup>1,3,4</sup> · Chunhui Xu<sup>1,2</sup> ·  
Vasyl Yurchyshyn<sup>4</sup>

© The author(s) ●●●●

**Abstract** Understanding and forecasting the geoeffectiveness of a coronal mass ejection (CME) is crucial for protecting infrastructure in the near-Earth space environment and on Earth. In this study, we present a novel fusion model to forecast the geoeffectiveness of CME events. Our model combines convolutional neural networks for feature learning and a prediction network for feature

---

✉ J.T.L. Wang  
[wangj@njit.edu](mailto:wangj@njit.edu)

✉ H. Wang  
[haimin.wang@njit.edu](mailto:haimin.wang@njit.edu)

Z. Yan  
[zy7@njit.edu](mailto:zy7@njit.edu)

H. Lee  
[harim.lee@njit.edu](mailto:harim.lee@njit.edu)

J. Jing  
[ju.jing@njit.edu](mailto:ju.jing@njit.edu)

Y. Xu  
[yan.xu@njit.edu](mailto:yan.xu@njit.edu)

C. Xu  
[cx4@njit.edu](mailto:cx4@njit.edu)

V. Yurchyshyn  
[vasyl.yurchyshyn@njit.edu](mailto:vasyl.yurchyshyn@njit.edu)

<sup>1</sup> Institute for Space Weather Sciences, New Jersey Institute of Technology, University Heights, Newark, NJ 07102, USA

<sup>2</sup> Department of Computer Science, New Jersey Institute of Technology, University Heights, Newark, NJ 07102, USA

<sup>3</sup> Center for Solar-Terrestrial Research, New Jersey Institute of Technology, University Heights, Newark, NJ 07102, USA

<sup>4</sup> Big Bear Solar Observatory, New Jersey Institute of Technology, 40386 North Shore Lane, Big Bear City, CA 92314, USA

---

fusion and event classification. The model is trained by observations from instruments including the Large Angle Spectroscopic Coronagraph (LASCO) on board the Solar and Heliospheric Observatory (SOHO) and the Atmospheric Imaging Assembly (AIA) and Helioseismic and Magnetic Imager (HMI) on board the Solar Dynamics Observatory (SDO). The trained model is then used to predict whether an Earth-reaching CME will cause a geomagnetic storm and/or the probability that the CME will cause such a storm. Experimental results based on a five-fold cross validation scheme demonstrate the good performance of our fusion model, achieving a mean true skill statistic (TSS) score of 0.703 when the model is used as a deterministic prediction tool, and a mean Brier score of 0.095 when the model is used as a probabilistic forecasting tool, where a TSS score of 1 or a Brier score of 0 indicates perfect performance. This work contributes to forecasting the causal relationship between Earth-directed CMEs and geomagnetic storms in solar-terrestrial interactions.

**Keywords:** Coronal mass ejections; Solar-terrestrial relations; Heliosphere

## 1. Introduction

Geomagnetic storms, often triggered by Earth-directed coronal mass ejections (CMEs; Liu, Webb, and Zhao 2006; Gopalswamy 2009; Vourlidas, Patsourakos, and Savani 2019; Zhang et al. 2025), pose significant threats to modern technological infrastructure in the near-Earth space environment and on Earth. These disturbances can compromise satellite operations, disrupt global positioning systems, interfere with radio communications, and induce harmful currents in power transmission networks. The severity of such storms is quantified through various geomagnetic indices, with the Dst (Disturbance Storm Time) index serving as a primary indicator, where Dst values below  $-50$  nT signify geomagnetic storm conditions (Gonzalez et al. 1994; Telloni 2022). Additional indices, including Kp, Ap, and high-resolution variants such as SYM-H and ASY-H, provide complementary storm characterization capabilities (Mayaud 1980; Wanliss and Showalter 2006).

Recently, the rapid advancement of artificial intelligence and machine learning has opened new avenues for forecasting the terrestrial effects of CMEs. For example, Besliu-Ionescu et al. (2019) adopted a logistic regression model to predict the geoeffectiveness of a given CME using CME parameters. Pricopi et al. (2022) extended the work of Besliu-Ionescu et al. (2019) by considering a suite of machine learning methods, including logistic regression, K-nearest neighbors (KNN), support vector machines (SVMs), feed-forward artificial neural networks (ANNs) and ensemble models, with solar onset parameters. Ye et al. (2025) developed a feature dimension reduction method in conjunction with a KNN model to predict the geoeffectiveness of CMEs using multiple CME features. Ye et al. (2024) investigated the geoeffectiveness of a CME and its dependence on solar wind conditions using an SVM model. Telloni et al. (2023) predicted geomagnetic events, also using solar wind data with multiple ANN models. Guastavino et al. (2024) formulated the prediction of geomagnetic disturbances as a binary

classification problem and employed a long short-term memory recurrent neural network, together with in situ measurements of solar wind plasma and magnetic field, to solve the problem. Hu, Camporeale, and Swiger (2023) designed multifidelity boosted neural networks, trained by solar wind parameters, to predict the Dst index. Liu et al. (2024) adopted a temporal convolutional network with integrated gradients to predict Dst. Fu et al. (2021) used solar images to predict the geoeffectiveness of CMEs with an attention-assisted convolutional neural network (CNN). Because only solar observations were used without handpicked features, their tool has the potential for making near-real-time forecasts.

In this study, we present a novel fusion model that combines convolutional neural networks for feature learning and a prediction network for feature fusion and event classification, to predict geoeffective CMEs. Specifically, we use observations collected by the Atmospheric Imaging Assembly (AIA; Lemen et al. 2012) and Helioseismic and Magnetic Imager (HMI; Scherrer et al. 2012) on board the Solar Dynamics Observatory (SDO; Pesnell, Thompson, and Chamberlin 2012) as well as the Large Angle Spectroscopic Coronagraph (LASCO; Brueckner et al. 1995) on board the Solar and Heliospheric Observatory (SOHO; Domingo, Fleck, and Poland 1995) to train and test our fusion model. The model predicts whether an Earth-reaching CME will cause a geomagnetic storm and/or the probability that the CME will cause such a storm, where the storm is defined as a disturbance of the Earth’s magnetosphere during which the minimum Dst value is lower than  $-50$  nT (Gonzalez et al. 1994; Telloni 2022). The fusion model achieves a mean true skill statistic (TSS) score of 0.703 when used as a deterministic prediction tool, and a mean Brier score of 0.095 when used as a probabilistic forecasting tool based on a five-fold cross validation scheme, where a TSS score of 1 or a Brier score of 0 indicates perfect predictions.

The remainder of this paper is organized as follows. Section 2 describes the observational data and pre-processing procedures used in our study. Section 3 presents the architecture and implementation details of our fusion model. Section 4 reports the experimental results obtained by evaluating the fusion model from the perspectives of deterministic prediction and probabilistic forecasting. Section 5 presents a discussion and concludes the paper.

## 2. Data

The main data source used in our study is the list of interplanetary CMEs maintained by Richardson and Cane (2010), referred to as the RC list. We selected 164 Earth-reaching CMEs that have LASCO observing time recorded in the RC list. These CME events spanned the period from 2011 to 2024. All selected CMEs were associated with Dst values in the RC list. Figure 1 shows the distribution of the Dst values for the 164 CMEs. A CME is geoeffective if its associated Dst value is lower than  $-50$  nT (Gonzalez et al. 1994; Telloni 2022). As a result, there were 86 geoeffective CMEs and 78 non-geoeffective CMEs. Figure 2 shows the breakdown of these CME events. The lower the Dst values, the stronger the corresponding geomagnetic storms.

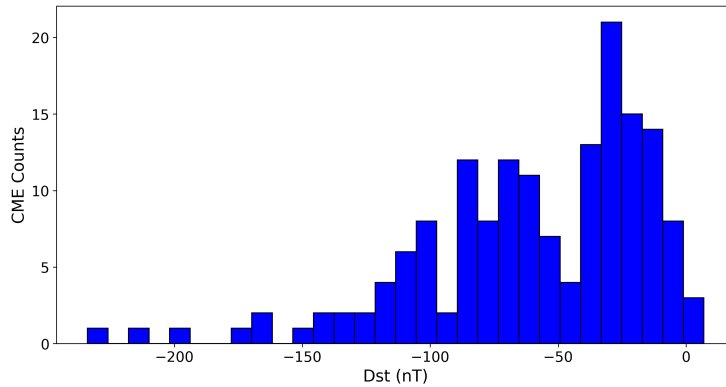


**Figure 1.** Distribution of the Dst index values for the 164 Earth-reaching CME events in our dataset.

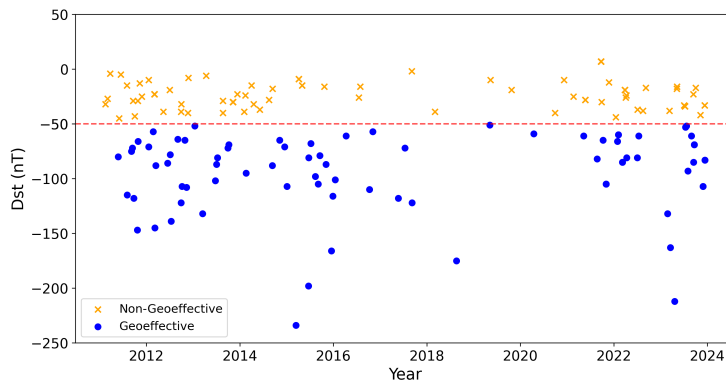


**Figure 2.** Breakdown of the geoeffective (blue) and non-geoeffective (orange) CME events in our dataset.

When training and validating our fusion model, we used solar observations from multiple instruments, including SOHO/LASCO, SDO/AIA with two channels 193 Å and 211 Å, and SDO/HMI. Figure 3 shows the solar observations on the CME event that occurred on 14 March 2015 UT, which are, from left to right, LASCO C2, AIA 193 Å, AIA 211 Å, and HMI. As in the literature (Wang et al. 2019; Alobaid et al. 2023), we used base-difference images for LASCO C2 to improve model performance. LASCO C2 images capture the early outward propagation of CMEs in the corona and provide onset signatures and initial speed estimates (Brueckner et al. 1995). AIA images show coronal dimmings and flare-related brightenings in the low corona that are strongly associated with CME initiation (Dissauer et al. 2018, 2019), and they also reveal coronal holes, which are the sources of high-speed solar wind streams that can interact with CMEs and affect their geoeffectiveness (Gopalswamy et al. 2009). HMI magnetograms provide the photospheric magnetic field context, including shear, polarity inversion lines, and sigmoidal structures, which are known to increase the probability of eruptions (Falconer, Moore, and Gary 2006; Toriumi and

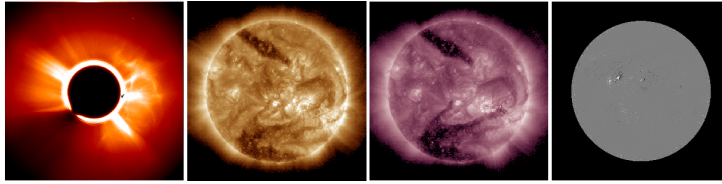


**Figure 3.** Solar observations on the CME event that occurred on 14 March 2015 UT. Shown from left to right are a LASCO C2 image, an AIA 193 Å image, an AIA 211 Å image, and a full-disk HMI line-of-sight magnetogram.

Wang 2019). Combining these observations gives a multimodal view of both the magnetic environment and the coronal response, improving the ability to assess CME potential and forecast their geoeffectiveness.

Each CME event in our dataset had a LASCO observing time stamp, denoted  $t$ , recorded in the RC list. Following Alobaid et al. (2024), we collected LASCO C2 images 10 minutes before  $t$  and 4 hours after  $t$ , averaging 21 images per CME event, with a total of 3,438 LASCO C2 images. In addition, we collected AIA 193 Å images and AIA 211 Å images, with a cadence of 1 hour, in the time window from 4 hours before  $t$  to  $t$ , totaling 1,295 AIA images. Finally, we collected HMI magnetograms, also with a cadence of 1 hour, in the time window from 3 hours before  $t$  to  $t$ , totaling 471 HMI magnetogram images. These temporal ranges were chosen on the basis of the literature (Alobaid et al. 2024) and also our own experimental study. We have tested larger temporal ranges, which incurred longer execution times without improving performance, and smaller temporal ranges, which yielded worse performance. Missing images in the time windows were excluded from the study. The dataset contained 5,204 images in total.

We then used a stratified 80:20 split on our CME event dataset for model training and testing. Specifically, we randomly selected 80% of the 86 geoeffective CME events in the dataset, which yielded 69 events, and 80% of the 78 non-geoeffective CME events in the dataset, which yielded 62 events, for model training. The remaining 20% from each class, including 17 geoeffective and 16 non-geoeffective events, were used for model testing. Thus, we maintained the same class proportions (geoeffective vs. non-geoeffective) in both training and test sets as the original event dataset. All images associated with an event were exclusively assigned to the same set, either training or test, to prevent data leakage. The training set and the test set are disjoint and, therefore, our trained model can make predictions on test data that it has never seen during training. To monitor model performance and prevent overfitting during training, we further selected 12% of the training events from each class and used the selected events for model validation.

### 3. Methodology

Figure 4 shows the architecture of our fusion model. The input of the fusion model consists of solar images associated with a CME event. Letting the LASCO

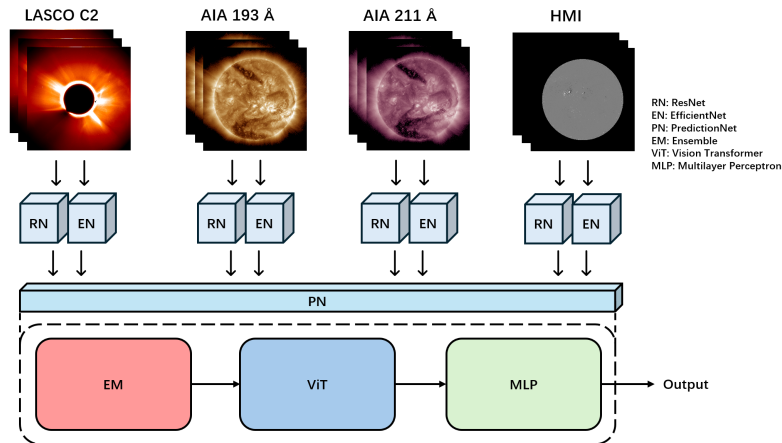


**Figure 4.** Overall architecture of our fusion model. The model accepts, as input, a CME event represented by images of four types (LASCO C2, AIA 193 Å, AIA 211 Å and HMI), and assigns a pair of networks, ResNet (RN) and EfficientNet (EN), to learn and extract features from the input images of each type. These learned features are then sent to our PredictionNet (PN), which is composed of three modules: ensemble (EM), vision transformer (ViT) and multilayer perceptron (MLP), for feature fusion and event classification. PN outputs “1” indicating that the input CME event is positive/geoeffective or “0” indicating that the input CME event is negative/non-geoeffective when our model is used as a deterministic prediction tool. When our model is used as a probabilistic forecasting tool, the output is a probability for the input CME event to be geoeffective.

observing time of the CME event be  $t$ , these solar images, which represent the CME event, include: 21 LASCO C2 images in the period from  $t - 10$  min to  $t + 4$  hr, 4 AIA 193 Å images and 4 AIA 211 Å images in the period from  $t - 4$  hr to  $t$ , and 3 HMI magnetograms in the period from  $t - 3$  hr to  $t$ .

We employ two convolutional neural networks (CNNs), specifically ResNet50 (He et al. 2016) and EfficientNet-B0 (Tan and Le 2019), for feature learning and a vision transformer (Dosovitskiy et al. 2021) for image classification based on learned features. CNNs are well known for their ability to learn useful features from raw pixel data. ResNet50 and EfficientNet-B0 are widely used CNNs due to their balance of performance and computational cost. Both ResNet50 and EfficientNet-B0 have been trained in ImageNet (Deng et al. 2009) and are adapted to our task through transfer learning (Pan and Yang 2010). Specifically, we load the pre-trained weights of ResNet50 and EfficientNet-B0 to our ResNet and EfficientNet models, respectively, and fine-tune the models using the training and validation images at hand. We assign a pair of ResNet and EfficientNet to each data type (LASCO C2, AIA 193 Å, AIA 211 Å and HMI), where the two CNNs are used to learn features from images of the respective data type.

For each data type, ResNet processes each image of that data type, individually and separately, through its deep residual architecture to produce a 2,048-channel feature map with a spatial dimension of  $7 \times 7$  pixels. The feature maps are intermediate representations produced by the convolutional layers in ResNet. Specifically, each data type has multiple images and hence is associated with multiple feature maps. For example, for the 21 LASCO C2 images,

we obtain 21 feature maps. These 21 feature maps are averaged to obtain a single representative 2,048-channel feature map with a spatial dimension of  $7 \times 7$  pixels. The average feature map preserves important temporal dynamics and fine-grained spatial features in the 21 LASCO C2 images. Similarly, for the 4 AIA 193 Å images (4 AIA 211 Å images, 3 HMI magnetogram images, respectively), we obtain 4 (4, 3, respectively) feature maps, which are averaged to obtain a single representative 2,048-channel feature map with a spatial dimension of  $7 \times 7$  pixels for the 4 AIA 193 Å images (4 AIA 211 Å images, 3 HMI magnetogram images, respectively). Simultaneously, EfficientNet uses its compound-scaled convolutional layers to produce a representative, average 1,280-channel feature map with the same spatial resolution of  $7 \times 7$  pixels for the multiple images of each data type. The representative, average feature maps of each data type are then sent to a prediction network, or PredictionNet (PN), which is composed of three modules: ensemble (EM), vision transformer (ViT) and multilayer perceptron (MLP).

For each data type, the EM module combines the two representative average feature maps produced by ResNet and EfficientNet, respectively, through channel concatenation and attention mechanisms to create a unified feature map of  $512 \times 7 \times 7$  pixels that preserves spatial information. This process results in four feature maps, one for each data type. Next, the EM module learns weights among the four feature maps to combine them to produce a final 512-dimensional feature map, which is projected onto a 768-dimensional space through a linear transformation to match the internal dimensionality requirements of the subsequent ViT module.

ViT is well known for its ability to classify images effectively. ViT transforms the processed 768-dimensional feature map into an optimized 512-dimensional feature vector. The MLP module has two fully connected layers: the first layer reduces dimensionality to 256 with ReLU activation, followed by dropout regularization with a dropout rate of 0.3 to prevent overfitting, and a final sigmoid-activated layer, which produces a probability for the input CME event to be geoeffective. To obtain deterministic predictions, we implement a probability threshold of 0.6 in our fusion model. CME events with predicted probabilities greater than or equal to the threshold are classified as geoeffective, while CME events with predicted probabilities below the threshold are classified as non-geoeffective. This threshold value was empirically optimized to balance recall and precision in our validation dataset. Specifically, the threshold of 0.6 was determined through a grid search on the validation set containing 9 geoeffective and 8 non-geoeffective CME events. We tested threshold values in the range between 0.3 and 0.7 with a step size of 0.05 and selected the threshold that maximized the true skill statistic (TSS), which will be defined in Section 4.1. TSS provides a balanced assessment of predictive skills that accounts for both the hit rate and the false alarm rate, independent of the class distribution (Bloomfield et al. 2012). The optimization was performed exclusively on the validation set to avoid data leakage from the test set.

Figure 5 details the ViT module, where we load the pre-trained weights of Dosovitskiy et al. (2021) into the module. The input 768-dimensional feature

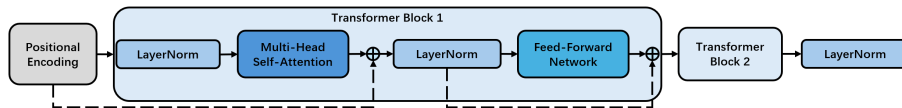


**Figure 5.** Architecture details of the vision transformer (ViT), which consists of multi-head self-attention layers, feed-forward networks, and residual connections for enhanced feature representation.

map with a spatial resolution of  $14 \times 14$  pixels is first partitioned into 196 non-overlapping patches by a positional encoding layer. This creates a sequence of 196 patch embeddings, each represented as a 768-dimensional vector. These patch embeddings are then processed through two sequential transformer encoder blocks, each containing a multi-head self-attention layer with 12 attention heads and a position-wise feed-forward network utilizing the GELU activation function. Residual connections, denoted by  $\oplus$ , and layer normalization ensure stable gradient flow and feature preservation throughout the transformer processing pipeline. The transformer blocks process the sequence of 196 patches, learning contextual relationships between the patches through the self-attention layers and feed-forward networks. Following transformer enhancement, the input 768-dimensional feature map undergoes a final layer normalization and is projected into an optimized 512-dimensional feature vector. Table 1 and Table 2 summarize the configuration and parameter details, respectively, of our fusion model.

**Table 1.** Configuration Details of the Proposed Fusion Model

Component	Configuration	Regularization	Activation	Output
ResNet	50 Layers	Batch Norm.	ReLU	$2,048 \times 7 \times 7$
EfficientNet	38 Layers	Batch Norm.	SiLU	$1,280 \times 7 \times 7$
EM Module	Conv2D + Attn.	Batch Norm.	ReLU	$512 \times 7 \times 7$
ViT Pos. Encoding	Linear Proj.	–	–	$196 \times 768$
ViT Trans. Block 1	12 Attn. Heads	Layer Norm.	GELU	$196 \times 768$
ViT Trans. Block 2	12 Attn. Heads	Layer Norm.	GELU	$196 \times 768$
MLP Dense Layer	Fully Connected	–	ReLU	256
MLP Output Layer	Fully Connected	Dropout (0.3)	Sigmoid	2

## 4. Experiments and Results

### 4.1. Experimental Setup

As mentioned in Section 2, we implemented a stratified data partitioning scheme by dividing the dataset at hand into training and test sets using an 80:20 ratio where approximately 12% of the training data from each class were selected for model validation. There were 164 CMEs in our dataset, with 86 being geoeffective and 78 being non-geoeffective. As a result, the training set had 69

**Table 2.** Parameter Analysis for the Proposed Fusion Model

Architecture Component	Layer Count	Trainable Parameters
ResNet	50	23.51M
EfficientNet	38	4.01M
EM Module	3	1.68M
ViT Transformer Enhancement	2 Blocks	14.37M
ViT Other Layers	3	0.89M
MLP Layers	2	0.20M
Whole Fusion Model	–	44.66M

geoeffective CMEs and 62 non-geoeffective CMEs where 9 geoeffective CMEs and 8 non-geoeffective CMEs are used for model validation, and the test set had 17 geoeffective CMEs and 16 non-geoeffective CMEs.

When evaluating our fusion model for deterministic prediction, we adopted five complementary performance metrics: recall, precision, accuracy, F1, and true skill statistic (TSS). Given a CME event  $E$ ,  $E$  is a true positive (TP) when the model predicts that  $E$  is positive (i.e. geoeffective) and  $E$  is indeed positive.  $E$  is a true negative (TN) when the model predicts that  $E$  is negative (i.e. non-geoeffective) and  $E$  is indeed negative.  $E$  is a false positive (FP) when the model predicts that  $E$  is positive while  $E$  is actually negative.  $E$  is a false negative (FN) when the model predicts that  $E$  is negative while  $E$  is actually positive. When the context is clear, we also use TP, TN, FP and FN to represent the total number of true positives, true negatives, false positives, and false negatives, respectively. The five performance metrics are mathematically defined as follows:

$$\text{Recall} = \frac{\text{TP}}{\text{TP} + \text{FN}}, \quad (1)$$

$$\text{Precision} = \frac{\text{TP}}{\text{TP} + \text{FP}}, \quad (2)$$

$$\text{Accuracy} = \frac{\text{TP} + \text{TN}}{\text{TP} + \text{FP} + \text{TN} + \text{FN}}, \quad (3)$$

$$\text{F1} = \frac{2 \times \text{TP}}{2 \times \text{TP} + \text{FP} + \text{FN}}, \quad (4)$$

$$\text{TSS} = \frac{\text{TP}}{\text{TP} + \text{FN}} - \frac{\text{FP}}{\text{FP} + \text{TN}}. \quad (5)$$

F1 combines precision and recall into a single value, providing a balanced measure of a model’s performance. TSS accounts for both the hit rate (recall) and the false alarm rate, providing a balanced assessment of predictive skills independent of the class distribution, as indicated previously. The F1 score ranges from 0 to 1, while the TSS score ranges from  $-1$  to 1, with a value of 1 indicating perfect model performance for both metrics.

In addition to the fusion model, we consider its three component networks alone, used as baseline methods. The ResNet baseline takes solar images as input from all four data types (LASCO C2, AIA 193 Å, AIA 211 Å, and HMI), which are first processed individually within their respective time windows. The resulting feature maps for each data type are averaged to obtain a single representative 2,048-channel feature map with a spatial dimension of  $7 \times 7$  pixels. Each data type yields an average feature map. The four average feature maps are then concatenated and fed into a multilayer perceptron (MLP) classifier, which has the same architecture as that used in the fusion model, to produce the output. The EfficientNet baseline works similarly. For the ViT baseline, the multiple images of each data type are first averaged to obtain a single representative image for each data type, respectively. Each average image is resized to  $112 \times 112$  pixels. The four resized average images are then concatenated into a  $224 \times 224$  image arranged in a  $2 \times 2$  grid. Next, the concatenated image is partitioned into  $14 \times 14 = 196$  non-overlapping patches, each having  $16 \times 16$  pixels. Each patch is linearly projected onto a 768-dimensional embedding vector, which matches the input dimensionality of the ViT baseline. These patch embeddings are then processed by two transformer encoder blocks with the same architecture as those shown in Figure 5, followed by an MLP classifier, which has the same architecture as that used in the fusion model, to produce the output. All three baseline methods and the proposed fusion model use the same training, validation, and test sets, as well as identical optimization settings, including the learning rate, batch size, number of epochs, and loss function, to ensure a fair and controlled comparison between the different models.

## 4.2. Deterministic Prediction Results

We conducted a series of experiments to evaluate the performance of the proposed fusion model and its component networks (i.e., the three baseline methods). Figure 6 presents the results. It can be seen in Figure 6 that the ViT baseline outperforms the other two component networks (ResNet and EfficientNet). Overall, the fusion model is the best, achieving a TSS score of 0.757. This happens probably because the fusion model combines the superior capabilities of convolutional neural networks in representation/feature learning and those of ViT for image recognition/classification. Previously, Alobaid et al. (2024) used different data and algorithms to predict geoeffective CMEs with a slightly lower TSS of 0.714, though a direct comparison between our work and Alobaid et al.'s work is not possible because the algorithms and datasets used by the two works differ.

Figure 7 presents the confusion matrix obtained by our fusion model. The confusion matrix provides a breakdown of errors that occur when the fusion model makes predictions on the test set. There are 33 CME events in the test set, with 17 being geoeffective/positive and 16 being non-geoeffective/negative. Among the 17 positive CME events, the fusion model correctly predicts 15 of them (TP = 15) and incorrectly predicts 2 of them to be negative, although the two are actually positive (FN = 2). Among the 16 negative CME events, the

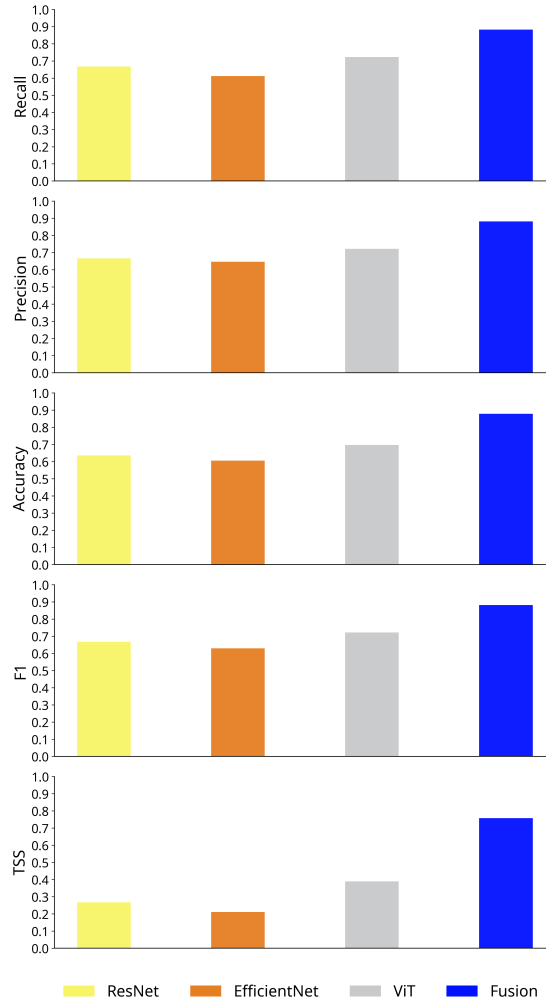


**Figure 6.** Comparison of our fusion model with its three component networks based on the 80:20 train-test split described in Section 2 when all the four tools are used for deterministic prediction. The fusion model achieves the best performance with a TSS score of 0.757.

fusion model correctly predicts 14 of them ( $TN = 14$ ) and incorrectly predicts 2 of them to be positive, although the two are actually negative ( $FP = 2$ ).

To ensure the statistical reliability of our performance assessment, we also performed a five-fold cross-validation experiment using stratified sampling to maintain consistent class distributions across all folds. Specifically, our dataset of 164 CME events was partitioned into five subsets of approximately equal size, each containing roughly 17 geoeffective and 16 non-geoeffective CMEs. The five-fold cross-validation was applied to all models, including the proposed fusion model and its component networks (i.e., the three baseline methods). With the five-fold cross validation, our fusion model achieved a mean TSS of 0.703, in reference to the mean TSS of 0.673 in Alobaid et al. (2024). The ResNet

TN 14	FP 2
FN 2	TP 15

**Figure 7.** The confusion matrix obtained by our fusion model used for deterministic prediction based on the 80:20 train-test split described in Section 2.

**Table 3.** Five-Fold Cross Validation Results of the Four Deterministic Prediction Models

Model	Recall	Precision	Accuracy	F1	TSS
ResNet	0.620±0.137	0.625±0.111	0.624±0.028	0.622±0.124	0.248±0.055
EfficientNet	0.565±0.174	0.604±0.149	0.598±0.030	0.584±0.162	0.195±0.060
ViT	0.674±0.089	0.684±0.072	0.681±0.024	0.679±0.081	0.363±0.048
Fusion	<b>0.819±0.035</b>	<b>0.876±0.030</b>	<b>0.851±0.015</b>	<b>0.847±0.033</b>	<b>0.703±0.030</b>

baseline achieved a mean TSS of 0.248, the EfficientNet baseline achieved a mean TSS of 0.195, and the ViT baseline achieved a mean TSS of 0.363. Table 3 presents the detailed results including the mean scores and standard deviations of all performance metrics, with the best metric values highlighted in boldface. The five-fold cross validation results again demonstrate the superiority of the proposed fusion model over the baseline methods.

There are four data types (LASCO C2, AIA 193 Å, AIA 211 Å and HMI) used as input to our fusion model. Figure 8 compares the effectiveness of the four data types and their combinations, including LASCO C2, AIA 193 Å, AIA 211 Å, HMI, LASCO C2 + AIA 193 Å, LASCO C2 + AIA 211 Å, LASCO C2 + HMI, AIA 193 Å + AIA 211 Å, AIA 193 Å + HMI, AIA 211 Å + HMI, LASCO C2 + AIA 193 Å + AIA 211 Å, LASCO C2 + AIA 193 Å + HMI, LASCO C2 + AIA 211 Å + HMI, AIA 193 Å + AIA 211 Å + HMI, LASCO C2 + AIA 193 Å + AIA 211 Å + HMI. Each data type alone is used as input to our model to produce results. Then, in turn, each combination is used as input to the model to produce the results. It can be seen in Figure 8 that combining the four data types together performs the best, achieving the highest TSS score of 0.757.

### 4.3. Model Interpretation

To elucidate the decision-making process of our fusion model, we employ Integrated Gradients (IG; Sundararajan, Taly, and Yan 2017), an axiomatic feature attribution method that explains deep learning model predictions by assigning



**Figure 8.** Comparison of the four data types (LASCO C2, AIA 193 Å, AIA 211 Å, HMI) and their combinations, each of which is used in turn as input to our fusion model, for deterministic prediction based on the 80:20 train-test split described in Section 2. The model achieves the best performance when all the four data types are used together.

importance scores to input features. The resulting attribution maps highlight the regions in the input images that most influence the model’s predictions. Based on Figure 8, AIA 193 Å and AIA 211 Å images have a stronger effect on the performance of our model than LASCO C2 and HMI images. Therefore, we use the two AIA images to explain the model’s decision-making process.

Figure 9 shows the AIA images and their corresponding IG attribution maps for a correctly predicted (true positive) CME event, denoted  $C$ , that occurred on 14 March 2015 UT (also see Figure 3). In each AIA image, the active region (AR) NOAA 12297, which is the source region of the event  $C$ , is highlighted

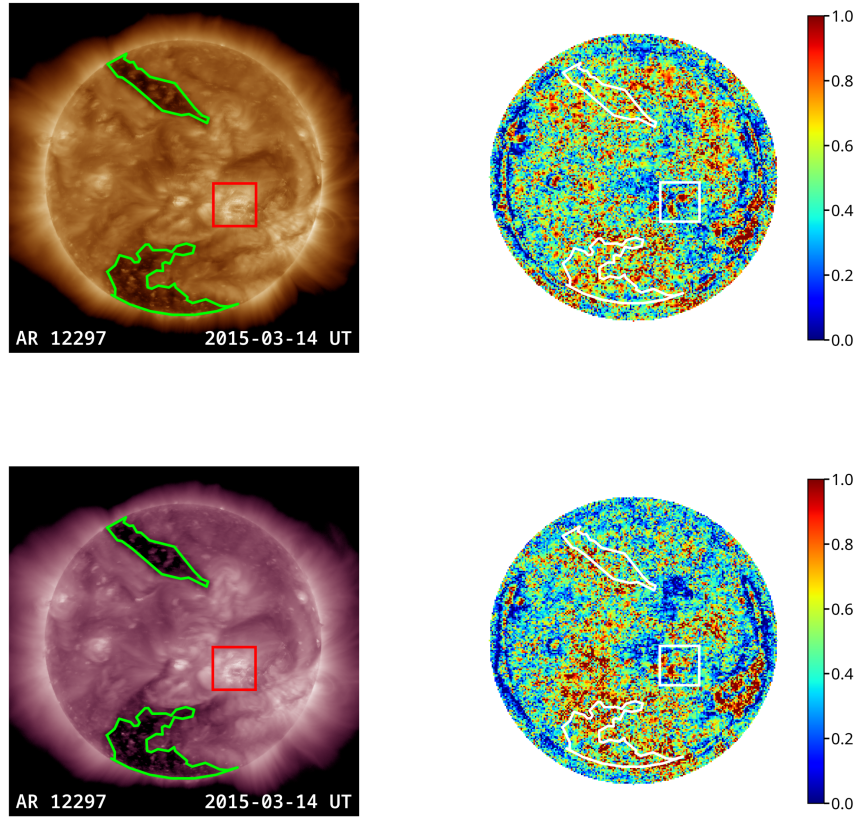


**Figure 9.** AIA 193 Å image (top), AIA 211 Å image (bottom), and their corresponding IG attribution maps for a correctly predicted (true positive) CME event that occurred on 14 March 2015 UT. The left column shows the AIA images and the right column shows the IG attribution maps. Each color bar indicates the normalized attribution intensity, ranging from 0 (blue, low attribution, low importance score) to 1 (red, high attribution, high importance score). In each AIA image, the AR 12297, which is the source region of the CME event, is highlighted by a red box, while the coronal holes are outlined in green. Based on the IG attribution maps, our fusion model assigns high importance scores to the coronal loops in the CME-producing AR 12297, paying much attention to the loops, and consequently predicts that the CME event is positive/geoeffective.

by a red box. This AR 12297 is identified by (1) locating all solar ARs and their coordinates at the appearance time of the event  $C$  using the Solar Region Summary provided by the Space Weather Prediction Center (SWPC),<sup>1</sup> (2) determining which of the ARs located in (1) produces a flare that may possibly be associated with a CME using the Geostationary Operational Environmental

<sup>1</sup><https://www.swpc.noaa.gov/products/solar-region-summary>

Satellite (GOES) X-ray flare catalogs provided by the National Centers for Environmental Information (NCEI), and (3) comparing the location (coordinates) of the AR identified in (2) with the location (central position angle) of the CME whose onset time recorded in the SOHO LASCO CME Catalog<sup>2</sup> matches, within a 2 hr window (Zhang et al. 2025), the appearance time of the event  $C$  to make sure that the AR identified in (2) is the source region of the event  $C$ . In addition, we extract the coronal holes and their locations (coordinates) in each AIA image from the Heliophysics Events Knowledgebase (Hurlburt et al. 2012) using SunPy (SunPy Community et al. 2015). The coronal holes in each AIA image are outlined in green. Separately, in each IG attribution map, the AR 12297 is highlighted by a white box, and the coronal holes are also outlined in white. In the attribution maps, warmer colors (red) indicate higher attribution values and cooler colors (blue) indicate lower attribution values. It can be seen in Figure 9 that our fusion model assigns high importance scores to the coronal loops in the CME-producing AR 12297, paying much attention to the loops, and consequently predicts that the CME event  $C$  is positive, i.e., it will cause a geomagnetic storm.

Figure 10 shows the AIA images and their corresponding IG attribution maps for an incorrectly predicted (false negative) CME event that occurred on 7 May 2019 UT. In each AIA image, the AR 12740, which is the source region of the CME event, is highlighted by a red box while the coronal holes are outlined in green. Separately, in each IG attribution map, the AR 12740 is highlighted by a white box, and the coronal holes are also outlined in white. This AR 12740 and coronal holes are located using the same methods as described above. It can be seen in Figure 10 that our fusion model does not pay sufficient attention to the coronal loops in the CME-producing AR 12740. As a result, the model predicts that the CME event is negative, though the CME event is actually positive, i.e., geoeffective.

#### 4.4. Probabilistic Forecasting Results

As explained in Figure 4, our fusion model can be used as a probabilistic forecasting tool, which outputs a probability that an input CME event will be geoeffective. The three component networks (ResNet, EfficientNet, and ViT) can also be used as probabilistic forecasting tools. When evaluating these networks for probabilistic forecasting, we adopted the Brier score (Brier 1950) and the Brier skill score (Wilks 2010). The Brier score, denoted BS, quantifies the accuracy of the probabilistic forecast by computing the mean squared difference between the predicted probabilities and actual binary outcomes, mathematically expressed as:

$$\text{BS} = \frac{1}{N} \sum_{i=1}^N (y_i - \hat{y}_i)^2, \quad (6)$$

---

<sup>2</sup>[https://cdaw.gsfc.nasa.gov/CME\\_list/](https://cdaw.gsfc.nasa.gov/CME_list/)

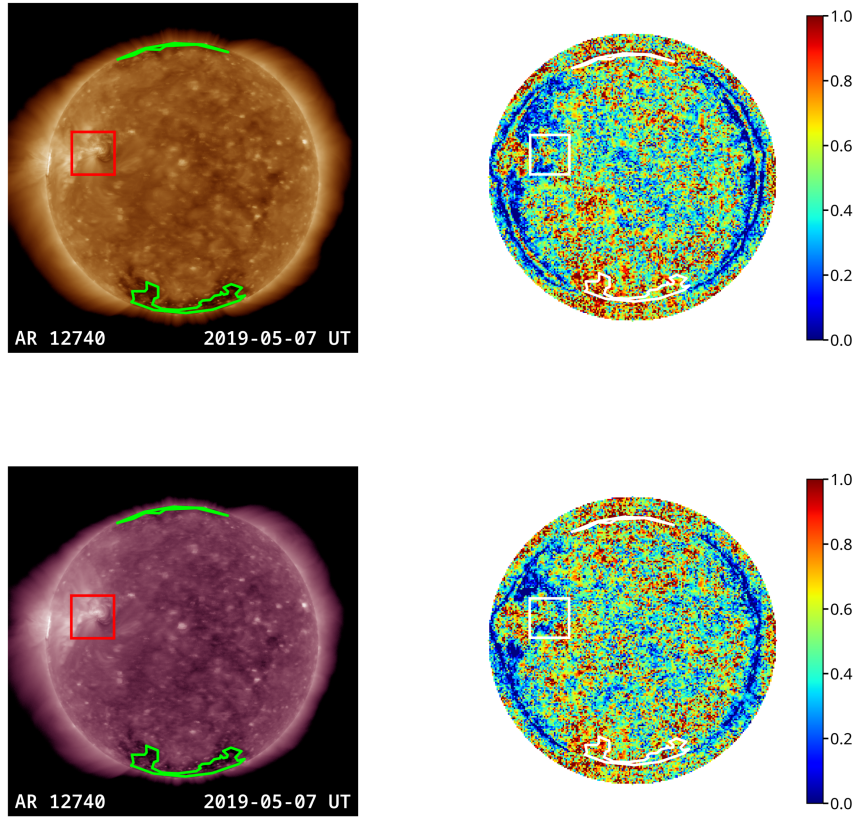


**Figure 10.** AIA 193 Å image (top), AIA 211 Å image (bottom), and their corresponding IG attribution maps for an incorrectly predicted (false negative) CME event that occurred on 7 May 2019 UT. In each AIA image, the AR 12740, which is the source region of the CME event, is highlighted by a red box, while the coronal holes are outlined in green. Based on the IG attribution maps, our fusion model does not pay sufficient attention to the coronal loops in the CME-producing AR 12740. Consequently, the model predicts that the CME event is negative, though the CME event is actually positive/geoeffective.

where  $N$  represents the total number of CME events in the test set,  $y_i$  denotes the actual binary outcome for the  $i$ th test event with 1 indicating that the event is geoeffective and 0 indicating that the event is non-geoeffective, and  $\hat{y}_i$  represents the predicted probability for the  $i$ th test event. Brier scores range from 0 to 1, with an optimal value of 0 representing perfect probabilistic accuracy.

The Brier skill score, denoted BSS, provides a normalized measure of model performance, calculated as:

$$\text{BSS} = 1 - \frac{\text{BS}}{\frac{1}{N} \sum_{i=1}^N (y_i - \bar{y})^2}, \quad (7)$$

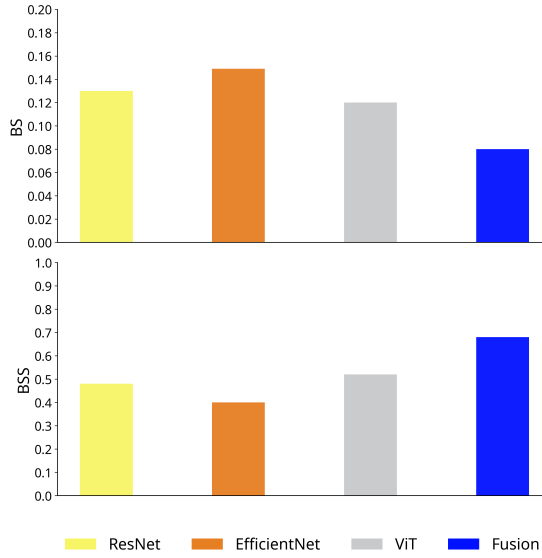


**Figure 11.** Comparison of our fusion model with its three component networks based on the 80:20 train-test split described in Section 2 when all the four tools are used for probabilistic forecasting. The fusion model achieves the best performance with a BS score of 0.080.

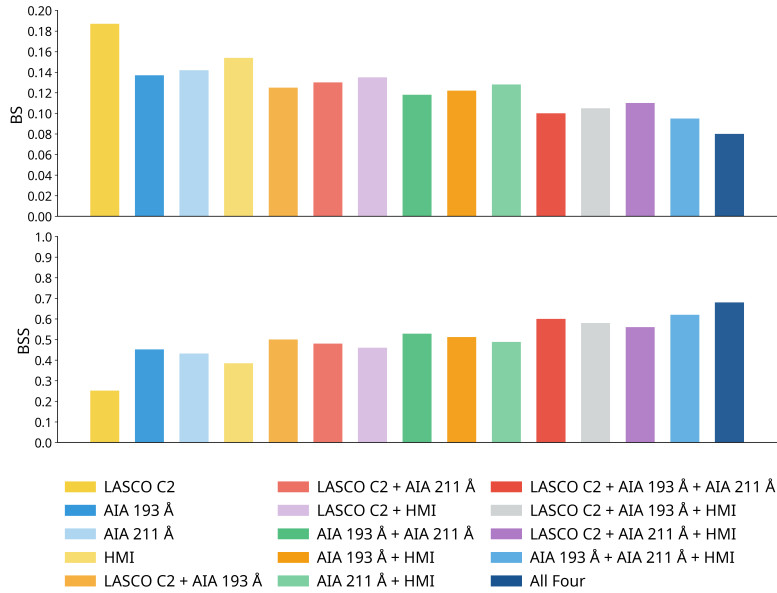
where  $\bar{y} = \frac{1}{N} \sum_{i=1}^N y_i$  represents the mean frequency of actual geoeffective events in the test set. BSS values range from  $-\infty$  to 1, with a perfect skill corresponding to  $BSS = 1$ .

Figure 11 compares the performance of the component networks (i.e., the three baseline methods) and the fusion model for probabilistic forecasting. Again, ViT performs better than the other two component networks (ResNet and EfficientNet). Overall, the fusion model is the best, achieving a BS score of 0.080, in reference to the BS score of 0.094 in Alobaid et al. (2024). To ensure the statistical reliability of our performance assessment, we also evaluated all models using five-fold cross-validation. Across the five folds, the fusion model achieved a mean BS score of 0.095, in reference to the mean BS score of 0.107 in Alobaid et al. (2024). The ResNet baseline achieved a mean BS score of 0.155, the EfficientNet baseline achieved a mean BS score of 0.179, and the ViT baseline achieved a mean BS score of 0.141. Table 4 presents the detailed results including the mean scores and standard deviations of the performance metrics, with the best metric values highlighted in boldface. Again, the fusion model outperforms its component networks.

Figure 12 compares the effectiveness of the four data types (LASCO C2, AIA 193 Å, AIA 211 Å and HMI) and their combinations for probabilistic forecasting. The results are consistent with those for the deterministic prediction shown in Figure 8 where combining the four data types together achieves the best performance.

**Table 4.** Five-Fold Cross-Validation Results of the Four Probabilistic Forecasting Models

Model	BS	BSS
ResNet	0.155±0.012	0.378±0.048
EfficientNet	0.179±0.015	0.282±0.060
ViT	0.141±0.011	0.435±0.044
Fusion	<b>0.095±0.010</b>	<b>0.619±0.040</b>

**Figure 12.** Comparison of the four data types (LASCO C2, AIA 193 Å, AIA 211 Å, HMI) and their combinations, each of which is used in turn as input to our fusion model, for probabilistic forecasting based on the 80:20 train-test split described in Section 2. The model achieves the best performance when all the four data types are used together.

## 5. Discussion and Conclusion

In this study, we proposed a new fusion model for predicting geoeffective CMEs, using data from Solar Cycles (SCs) 24 and 25 to train the model. Specifically, the model uses four types of solar images (LASCO C2, AIA 193 Å, AIA 211 Å and HMI) and combines three state-of-the-art neural networks (ResNet, EfficientNet, and ViT) for feature learning, feature fusion, image classification, and event prediction. With five-fold cross validation, the model achieves a mean true skill statistic (TSS) score of 0.703 when used as a deterministic prediction tool and a mean Brier score of 0.095 when used as a probabilistic forecasting tool, in reference to the mean TSS score of 0.673 and the mean Brier score of 0.107 in Alobaid et al. (2024), who used training data collected in SC 23. Notice that, as in the work of Alobaid et al. (2024), we rely on existing tools (e.g., Sudar,

Vršnak, and Dumbović 2016; Liu et al. 2018; Wang et al. 2019; Amerstorfer et al. 2021; Dumbović et al. 2021; Kaportseva and Shugay 2021; Alobaid et al. 2022; Baratashvili et al. 2022; Guastavino et al. 2023; Chierichini et al. 2024; Ye et al. 2024; Chen et al. 2025; Pattnaik, Michalek, and Ravishankar 2025) to predict whether a CME event will arrive at Earth. If it is predicted that the CME will hit Earth, then one can use the fusion model developed here to further predict whether the CME will cause a geomagnetic storm and/or the probability that the CME will cause such a storm.

Our work uses AIA images and HMI magnetograms. In practice, AIA images can be saturated, which causes pixels to lose detail, making it difficult to see the underlying structures (Schwartz, Torre, and Piana 2014; Guastavino et al. 2019; Yu et al. 2022). Saturation occurs when large solar flares and coronal mass ejections produce intense bursts of EUV light that saturate the detector. Saturation can be resolved by using de-saturation tools, which reconstruct lost information (Schwartz et al. 2015; Yu et al. 2022). In our dataset, there are 740 AIA 193 Å images each with  $4,096 \times 4,096$  pixels; 64.5% of the images (i.e., 477 images) have no saturated pixel. Among the remaining 263 images having saturated pixels, 33 images contain more than 100 saturated pixels (out of the total  $4,096 \times 4,096 = 16,777,216$  pixels); no image contains more than 1,000 saturated pixels. There are 646 AIA 211 Å images each with  $4,096 \times 4,096$  pixels (missing images were excluded from the study as mentioned in Section 2); 81.9% of the images (i.e., 529 images) have no saturated pixel. Among the remaining 117 images having saturated pixels, 31 images contain more than 100 saturated pixels, 12 images contain more than 1,000 saturated pixels, and 2 images contain more than 10,000 saturated pixels with one image containing 10,277 saturated pixels and the other image containing 11,506 saturated pixels. These statistics show that saturated pixels account for a small portion of the AIA images used in the study. In addition, 93.5% of the AIA 193 Å images have an exposure time more than 1.0 second, and 91.1% of the images have an exposure time more than 2.0 seconds. There are 5 AIA 193 Å images with an exposure time less than 0.2 seconds. By contrast, all the AIA 211 Å images have an exposure time more than 2.0 seconds. How saturated and/or short-exposure images influence the prediction of geoeffective CMEs and how to explain the influence using IG attribution maps will be further investigated in future work.

Our experimental results based on the 80:20 train-test split and five-fold cross validation showed that the proposed fusion model performs better than all baseline methods. On the basis of these experimental results, we conclude that the fusion model is a feasible tool for predicting geoeffective CMEs. Because the proposed model is trained by observations collected in the current solar cycle and the testing SOHO LASCO C2 images as well as the SDO observations can be obtained in near real-time, the proposed model has the potential to be an operational near real-time forecasting system.

**Acknowledgments** We acknowledge constructive suggestions and comments from an anonymous referee that have helped to significantly improve the manuscript. We also thank members of the Institute for Space Weather Sciences for fruitful discussions. The SOHO LASCO CME Catalog is generated and maintained at the CDAW Data Center by NASA and The Catholic

University of America in cooperation with the Naval Research Laboratory. SDO is a NASA mission to observe solar activity and space weather. SOHO is an international cooperation project between ESA and NASA.

**Author Contribution** J.W. and H.W. conceived the study. Z.Y. wrote the manuscript. All the authors reviewed the manuscript.

**Funding** J.W. and H.W. acknowledge support from NSF AGS grants 2228996, 2149748, NSF OAC grants 2504860, 2320147, and NASA grants 80NSSC24K0548, 80NSSC24K0843, 80NSSC24M0174. J.J. acknowledges support from NSF AGS grants 2300341, 2149748. Y.X. acknowledges support from NSF AGS grants 2228996, 2229064, and NSF RISE-2425602 grant. V.Y. acknowledges support from NSF AGS grants 2401229, 2408174, 2300341, 2309939, NSF AST-2108235 grant, and NASA 80NSSC24K1914 grant.

**Data Availability** CME events used in this study were compiled from the RC list in <https://izw1.caltech.edu/ACE/ASC/DATA/level3/icmetable2.htm>. SOHO LASCO C2 images were collected from the SOHO science archives at <https://soho.nascom.nasa.gov/data/archive/>. SDO observations were collected from the Joint Science Operations Center (JSOC) at <http://jsoc.stanford.edu/>.

## Declarations

**Conflict of interest** The authors declare no conflict of interest.

## References

- Alobaid, K.A., Abdullah, Y., Wang, J.T.L., Wang, H., Jiang, H., Xu, Y., Yurchyshyn, V., Zhang, H., Cavus, H., Jing, J.: 2022, Predicting CME arrival time through data integration and ensemble learning. *Frontiers in Astronomy and Space Sciences* **9**, 1013345. DOI.
- Alobaid, K.A., Abdullah, Y., Wang, J.T.L., Wang, H., Fan, S., Li, J., Cavus, H., Yurchyshyn, V.: 2023, Estimating coronal mass ejection mass and kinetic energy by fusion of multiple deep-learning models. *Astrophys. J. Lett.* **958**, L34. DOI.
- Alobaid, K.A., Wang, J.T.L., Wang, H., Jing, J., Abdullah, Y., Wang, Z., Farooki, H., Cavus, H., Yurchyshyn, V.: 2024, Prediction of geoeffective CMEs using SOHO images and deep learning. *Sol. Phys.* **299**, 159. DOI.
- Amerstorfer, T., Hinterreiter, J., Reiss, M.A., Möstl, C., Davies, J.A., Bailey, R.L., Weiss, A.J., Dumbović, M., Bauer, M., Amerstorfer, U.V., Harrison, R.A.: 2021, Evaluation of CME arrival prediction using ensemble modeling based on heliospheric imaging observations. *Space Weather* **19**, e02553. DOI.
- Baratashvili, T., Verbeke, C., Wijsen, N., Poedts, S.: 2022, Improving CME evolution and arrival predictions with AMR and grid stretching in Icarus. *Astron. Astrophys.* **667**, A133. DOI.
- Besliu-Ionescu, D., Talpeanu, D.-C., Mierla, M., Maris Muntean, G.: 2019, On the prediction of geoeffectiveness of CMEs during the ascending phase of SC24 using a logistic regression method. *J. Atmos. Solar-Terr. Phys.* **193**, 105036. DOI.
- Bloomfield, D.S., Higgins, P.A., McAteer, R.T.J., Gallagher, P.T.: 2012, Toward reliable benchmarking of solar flare forecasting methods. *Astrophys. J. Lett.* **747**, L41. DOI.
- Brier, G.W.: 1950, Verification of forecasts expressed in terms of probability. *Monthly Weather Review* **78**, 1. DOI.
- Brueckner, G.E., Howard, R.A., Koomen, M.J., Korendyke, C.M., Michels, D.J., Moses, J.D., Socker, D.G., Dere, K.P., Lamy, P.L., Llebaria, A., Bout, M.V., Schwenn, R., Simnett, G.M., Bedford, D.K., Eyles, C.J.: 1995, The Large Angle Spectroscopic Coronagraph (LASCO). *Sol. Phys.* **162**, 357. DOI.
- Chen, H., Sachdeva, N., Huang, Z., Holst, B., Manchester, W., Jivani, A., Zou, S., Chen, Y., Huan, X., Toth, G.: 2025, Decent estimate of CME arrival time from a data-assimilated ensemble in the Alfvén Wave Solar atmosphere Model (DECADE-AWSOM). *Space Weather* **23**, 2024SW004165. DOI.

- Chierichini, S., Liu, J., Korsós, M.B., Del Moro, D., Erdélyi, R.: 2024, CME arrival modeling with machine learning. *Astrophys. J.* **963**, 121. DOI.
- Deng, J., Dong, W., Socher, R., Li, L.-J., Li, K., Fei-Fei, L.: 2009, ImageNet: A large-scale hierarchical image database. In: *Proceedings of the IEEE Conference on Computer Vision and Pattern Recognition*, 248. DOI.
- Dissauer, K., Veronig, A.M., Temmer, M., Podladchikova, T., Vanninathan, K.: 2018, Statistics of coronal dimmings associated with coronal mass ejections. I. Characteristic dimming properties and flare association. *Astrophys. J.* **863**, 169. DOI.
- Dissauer, K., Veronig, A.M., Temmer, M., Podladchikova, T.: 2019, Statistics of coronal dimmings associated with coronal mass ejections. II. Relationship between coronal dimmings and their associated CMEs. *Astrophys. J.* **874**, 123. DOI.
- Domingo, V., Fleck, B., Poland, A.I.: 1995, The SOHO mission: An overview. *Sol. Phys.* **162**, 1. DOI.
- Dosovitskiy, A., Beyer, L., Kolesnikov, A., Weissenborn, D., Zhai, X., Unterthiner, T., Dehghani, M., Minderer, M., Heigold, G., Gelly, S., Uszkoreit, J., Hounsby, N.: 2021, An image is worth 16x16 words: Transformers for image recognition at scale. In: *Proceedings of the 9th International Conference on Learning Representations*.
- Dumbović, M., Čalogović, J., Martinić, K., Vršnak, B., Sudar, D., Temmer, M., Veronig, A.: 2021, Drag-based model (DBM) tools for forecast of coronal mass ejection arrival time and speed. *Front. Astron. Space Sci.* **8**, 58. DOI.
- Falconer, D.A., Moore, R.L., Gary, G.A.: 2006, Magnetic causes of solar coronal mass ejections: Dominance of the free magnetic energy over the magnetic twist alone. *Astrophys. J.* **644**, 1258. DOI.
- Fu, H., Zheng, Y., Ye, Y., Feng, X., Liu, C., Ma, H.: 2021, Joint geoeffectiveness and arrival time prediction of CMEs by a unified deep learning framework. *Remote Sens.* **13**, 1738. DOI.
- Gonzalez, W.D., Joselyn, J.A., Kamide, Y., Kroehl, H.W., Rostoker, G., Tsurutani, B.T., Vasyliunas, V.M.: 1994, What is a geomagnetic storm? *J. Geophys. Res.* **99**, 5771. DOI.
- Gopalswamy, N.: 2009, Halo coronal mass ejections and geomagnetic storms. *Earth, Planets and Space* **61**, 595. DOI.
- Gopalswamy, N., Mäkelä, P., Xie, H., Akiyama, S., Yashiro, S.: 2009, CME interactions with coronal holes and their interplanetary consequences. *Journal of Geophysical Research (Space Physics)* **114**, A00A22. DOI.
- Guastavino, S., Piana, M., Massone, A.M., Schwartz, R., Benvenuto, F.: 2019, Desaturating SDO/AIA observations of solar flaring storms. *Astrophys. J.* **882**, 109. DOI.
- Guastavino, S., Candiani, V., Bemporad, A., Marchetti, F., Benvenuto, F., Massone, A.M., Mancuso, S., Susino, R., Telloni, D., Fineschi, S., Piana, M.: 2023, Physics-driven machine learning for the prediction of coronal mass ejections' travel times. *Astrophys. J.* **954**, 151. DOI.
- Guastavino, S., Bahamazava, K., Perracchione, E., Camattari, F., Audone, G., Telloni, D., Susino, R., Nicolini, G., Fineschi, S., Piana, M., Massone, A.M.: 2024, Forecasting geoeffective events from solar wind data and evaluating the most predictive features through machine learning approaches. *Astrophys. J.* **971**, 94. DOI.
- He, K., Zhang, X., Ren, S., Sun, J.: 2016, Deep residual learning for image recognition. In: *Proceedings of the IEEE Conference on Computer Vision and Pattern Recognition*, 770. DOI.
- Hu, A., Camporeale, E., Swiger, B.: 2023, Multi-hour-ahead Dst index prediction using multi-fidelity boosted neural networks. *Space Weather* **21**. DOI.
- Hurlburt, N., Cheung, M., Schrijver, C., Chang, L., Freeland, S., Green, S., Heck, C., Jaffey, A., Kobashi, A., Schiff, D., Serafin, J., Seguin, R., Slater, G., Somani, A., Timmons, R.: 2012, Heliophysics Event Knowledgebase for the Solar Dynamics Observatory (SDO) and beyond. *Sol. Phys.* **275**, 67. DOI.
- Kaportseva, K.B., Shugay, Y.S.: 2021, Use of the DBM model to the predict of arrival of coronal mass ejections to the Earth. *Cosmic Res.* **59**, 268. DOI.
- Lemen, J.R., Title, A.M., Akin, D.J., Boerner, P.F., Chou, C., Drake, J.F., Duncan, D.W., Edwards, C.G., Friedlaender, F.M., Heyman, G.F., Hurlburt, N.E., Katz, N.L., Kushner, G.D., Levay, M., Lindgren, R.W., Mathur, D.P., McFeaters, E.L., Mitchell, S., Rehse, R.A., Schrijver, C.J., Springer, L.A., Stern, R.A., Tarbell, T.D., Wuelsel, J.-P., Wolfson, C.J., Yanari, C., Bookbinder, J.A., Cheimets, P.N., Caldwell, D., Deluca, E.E., Gates, R., Golub, L., Park, S., Podgorski, W.A., Bush, R.I., Scherrer, P.H., Gummin, M.A., Smith, P., Aufer, G., Jerram, P., Pool, P., Soufli, R., Windt, D.L., Beardsley, S., Clapp, M., Lang, J., Waltham,

- N.: 2012, The Atmospheric Imaging Assembly (AIA) on the Solar Dynamics Observatory (SDO). *Sol. Phys.* **275**, 17. DOI.
- Liu, J., Ye, Y., Shen, C., Wang, Y., Erdélyi, R.: 2018, A new tool for CME arrival time prediction using machine learning algorithms: CAT-PUMA. *Astrophys. J.* **855**, 109. DOI.
- Liu, J., Shen, C., Wang, Y., Xu, M., Chi, Y., Zhong, Z., Mao, D., Zhang, Z., Wang, C., Liu, J., Wang, Y.: 2024, Forecasting the Dst index with temporal convolutional network and integrated gradients. *Sol. Phys.* **299**, 98. DOI.
- Liu, Y., Webb, D.F., Zhao, X.P.: 2006, Magnetic structures of solar active regions, full-halo coronal mass ejections, and geomagnetic storms. *Astrophys. J.* **646**, 1335. DOI.
- Mayaud, P.N.: 1980, What is a geomagnetic index? In: *Derivation, Meaning, and Use of Geomagnetic Indices*, American Geophysical Union. Chap. 2. DOI.
- Pan, S.J., Yang, Q.: 2010, A survey on transfer learning. *IEEE Trans. Knowl. Data Eng.* **22**, 1345. DOI.
- Pattnaik, A., Michalek, G., Ravishankar, A.: 2025, Estimation of transit time of CMEs from the Sun to Earth. *Astrophys. J.* **982**, 35. DOI.
- Pesnell, W.D., Thompson, B.J., Chamberlin, P.C.: 2012, The Solar Dynamics Observatory (SDO). *Sol. Phys.* **275**, 3. DOI.
- Pricopi, A.-C., Paraschiv, A.R., Besliu-Ionescu, D., Marginean, A.-N.: 2022, Predicting the geoeffectiveness of CMEs using machine learning. *Astrophys. J.* **934**, 176. DOI.
- Richardson, I.G., Cane, H.V.: 2010, Near-Earth interplanetary coronal mass ejections during solar cycle 23 (1996 - 2009): Catalog and summary of properties. *Sol. Phys.* **264**, 189. DOI.
- Scherrer, P.H., Schou, J., Bush, R.I., Kosovichev, A.G., Bogart, R.S., Hoeksema, J.T., Liu, Y., Duvall, T.L., Zhao, J., Title, A.M., Schrijver, C.J., Tarbell, T.D., Tomczyk, S.: 2012, The Helioseismic and Magnetic Imager (HMI) investigation for the Solar Dynamics Observatory (SDO). *Sol. Phys.* **275**, 207. DOI.
- Schwartz, R.A., Torre, G., Piana, M.: 2014, Systematic de-saturation of images from the Atmospheric Imaging Assembly in the Solar Dynamics Observatory. *Astrophys. J. Lett.* **793**, L23. DOI.
- Schwartz, R.A., Torre, G., Massone, A.M., Piana, M.: 2015, DESAT: A Solar SoftWare tool for image de-saturation in the Atmospheric Image Assembly onboard the Solar Dynamics Observatory. *Astronomy and Computing* **13**, 117. DOI.
- Sudar, D., Vršnak, B., Dumbović, M.: 2016, Predicting coronal mass ejections transit times to Earth with neural network. *Mon. Not. R. Astron. Soc.* **456**, 1542. DOI.
- Sundararajan, M., Taly, A., Yan, Q.: 2017, Axiomatic attribution for deep networks. In: *Proceedings of the 34th International Conference on Machine Learning*, 3319.
- SunPy Community, Mumford, S.J., Christe, S., Pérez-Suárez, D., Ireland, J., Shih, A.Y., Inglis, A.R., Liedtke, S., Hewett, R.J., Mayer, F., Hughitt, K., Freij, N., Meszaros, T., Bennett, S.M., Malocha, M., Evans, J., Agrawal, A., Leonard, A.J., Robitaille, T.P., Mampaey, B., Campos-Rozo, J.L., Kirk, M.S.: 2015, SunPy—Python for solar physics. *Computational Science and Discovery* **8**, 014009. DOI.
- Tan, M., Le, Q.V.: 2019, EfficientNet: Rethinking model scaling for convolutional neural networks. In: *Proceedings of the 36th International Conference on Machine Learning* **97**, 6105.
- Telloni, D.: 2022, Statistical methods applied to space weather science. *Front. Astron. Space Sci.* **9**, 865880. DOI.
- Telloni, D., Schiavo, M.L., Magli, E., Fineschi, S., Guastavino, S., Nicolini, G., Susino, R., Giordano, S., Amadori, F., Candiani, V., Massone, A.M., Piana, M.: 2023, Prediction capability of geomagnetic events from solar wind data using neural networks. *Astrophys. J.* **952**, 111. DOI.
- Toriumi, S., Wang, H.: 2019, Flare-productive active regions. *Living Reviews in Solar Physics* **16**, 3. DOI.
- Vourlidas, A., Patsourakos, S., Savani, N.P.: 2019, Predicting the geoeffective properties of coronal mass ejections: current status, open issues and path forward. *Philosophical Transactions of the Royal Society A* **377**, 20180096. DOI.
- Wang, Y., Liu, J., Jiang, Y., Erdélyi, R.: 2019, CME arrival time prediction using convolutional neural network. *Astrophys. J.* **881**, 15. DOI.
- Wanliss, J.A., Showalter, K.M.: 2006, High-resolution global storm index: Dst versus SYM-H. *J. Geophys. Res. (Space Physics)* **111**, A02202. DOI.
- Wilks, D.S.: 2010, Forecast verification. In: *Statistical Methods in the Atmospheric Sciences*, 3rd edn., Elsevier. Chap. 8. DOI.

- Ye, D., Li, H., Guo, L., Jiang, X.: 2025, An improved halo coronal mass ejection geoeffectiveness prediction model using multiple coronal mass ejection features based on the DC-PCA-KNN method. *Astrophys. J.* **978**, 66. [DOI](#).
- Ye, Y., Liu, J., Hao, Y., Cui, J.: 2024, Evaluating the geoeffectiveness of interplanetary coronal mass ejections: Insights from a support vector machine approach with SHAP value analysis. *Astrophys. J.* **972**, 52. [DOI](#).
- Yu, X., Xu, L., Ren, Z., Zhao, D., Sun, W.: 2022, Image desaturation for SDO/AIA using mixed convolution network. *Research in Astronomy and Astrophysics* **22**, 065009. [DOI](#).
- Zhang, H., Jing, J., Wang, J.T.L., Wang, H., Abdullah, Y., Xu, Y., Alobaid, K.A., Farooki, H., Yurchyshyn, V.: 2025, Prediction of halo coronal mass ejections using SDO/HMI vector magnetic data products and a transformer model. *Astrophys. J.* **981**, 37. [DOI](#).